PCCP

Accepted Manuscript

ROYAL SOCIETY OF CHEMISTRY

www.rsc.org/pccp

CREATED USING THE RSC LaTeX PCCP ARTICLE TEMPLATE – SEE www.rsc.org/electronicfiles FOR DETAILS

ARTICLE TYPE www. rsc.org/xxxxxx | XXXXXXXX

Synthesis, characterization and theoretical studies of the nonlinear optical crystal $Sr_2B_5O_9(OH)\cdot H_2O$†

Fangyuan Zhang,[a,b] Fangfang Zhang,*[b] Jing Qun,[b] Shilie Pan,*[b] Zhihua Yang[b] and Dianzeng Jia[a]

Received Xth XXXXXXXXXX 20XX, Accepted Xth XXXXXXXXX 20XX

First published on the web Xth XXXXXXXXXX 200X

DOI: 10.1039/b000000x

The strontium borate $Sr_2B_5O_9(OH)\cdot H_2O$ (space group *C*2, No. 5) has been synthesized in high yields by a facile hydrothermal method. The UV-Vis-NIR diffuse reflectance spectrum shows that it has a wide transparency range extending from UV to NIR with the short-wavelength cut off edge below 190 nm. Second-harmonic generation (SHG) has been measured with a 1064 nm laser using the Kurtz and Perry technique, which shows that $Sr_2B_5O_9(OH)\cdot H_2O$ is phase matchable and the powder SHG effect is approximately 3 times that of KDP. It also has a high thermal stability up to 500 °C which has been identified by TG, DSC and variable-temperature PXRD. These properties make it possible for application as a UV nonlinear optical (NLO) material. On the basis of the electronic band structure, the optical refractive indices, birefringence, and SHG coefficients of $Sr_2B_5O_9(OH)\cdot H_2O$ are calculated, which are consistent with experiments. In addition, the electronic structure, SHG-weighted electron density and real-space atom-cutting analyses are performed to elucidate the origin of its NLO property.

1 Introduction

In recent years, UV NLO crystals have gained considerable attention due to their important roles in the solid-state laser to generate UV coherent light by direct SHG process. Continuous intensive studies have focused on design and synthesis UV NLO materials. Besides the several crystals that have been well developed or practically used in lasers,[1–5] a series of new compounds exhibiting good UV NLO properties have been explored from different systems of beryllium borate (fluoride),[6] borate halide,[7,8] borosilicate (halide),[9] rare earth borate,[10] carbonate (fluoride),[11] and phosphate (halide),[12] etc. From the practical viewpoint, searching for crystals with improved performances, including large SHG effect, wide transparency window, moderate birefringence, high stability and good growth habit, etc., is necessary and still ongoing.

Acentric structures have attracted significant interest for their potentiality as NLO crystals because bulk second-order NLO susceptibility is a third-rank tensor and will vanish in a centrosymmetric media.[13,14] In an attempt to explore compounds that are potentially applicable as UV NLO materials, we chose to grow strontium borate crystals by mild hydrothermal method. It is of special interest for exploring UV NLO materials in this system because the π-conjugated system based on the BO_3 group is a factor that favors acentric structure.[15] Other favorable features include the structural versatilities derived from the different combination types of the BO_3 and BO_4 groups,[16–19] as well as the UV transparency of the basic structural units (strontium polyhedra, borate groups and hydroxyl groups) that usually connected each other through small electrostatic interactions in strontium borates. To date, about a dozen strontium borates have been synthesized and structurally determined,[20–29] and of these, only several crystals are acentric, which satisfy the critical prerequisite requirement for bulk NLO activity. α-SrB_4O_7 has been explored to have very high effective NLO coefficient; however, the birefringence of α-SrB_4O_7 is too small to realize phase matching for SHG.[25] $Sr_4B_{14}O_{25}$ has been studied to be a very suitable host lattice for luminescence of lanthanide ions.[26] The crystal $Sr_2B_6O_9(OH)_4$ is a new phase in the strontium borate system and exhibits an SHG response of approximately 1.5 times that of KDP.[27] Very recently, we reported the investigations of the new strontium borate, $Sr_4B_{10}O_{18}(OH)_2\cdot 2H_2O$ (space group *P*1, No. 1), which exhibits a powder SHG response of approximately 2 times that of KDP.[28] A continuous effort in the strontium borate system has led to the title compound, $Sr_2B_5O_9(OH)\cdot H_2O$. The synthesis and crystal structure of $Sr_2B_5O_9(OH)\cdot H_2O$ was first reported by Barbier,[29] and recently, reexamined by Yang, et al.[27] In this pa-

† Electronic Supplementary Information (ESI) available: CIF (CCDC NO. 1038379); single crystal X-ray diffraction measurement; tables of crystal data and structural refinement, atomic coordinates, and selected bond lengths and angles; photograph of the crystal; IR spectrum; Mulliken analysis and electron densities. See DOI: 10.1039/b000000x/

[a] *College of Chemistry and Chemical Engineering, Xinjiang University, Urumqi 830046, China*

[b] *Key Laboratory of Functional Materials and Devices for Special Environments, Xinjiang Technical Institute of Physics and Chemistry, Chinese Academy of Sciences, Xinjiang Key Laboratory of Electronic Information Materials and Devices, 40-1 South Beijing Road, Urumqi 830011, China. E-mails: ffzhang@ms.xjb.ac.cn, slpan@ms.xjb.ac.cn. Tel: +86-(0)991-3674558; Fax: +86-(0)991-3838957*

per, we focus on the high yield synthesis and the comprehensive characterizations of the linear- and nonlinear-optical properties that are important for the application as a UV NLO crystal. In addition, theoretical studies were carried out to deepen the understanding of the origins of the optical properties. The electronic structure calculation, SHG-weighted electron density and real-space atom-cutting analyses demonstrate that the SHG response is mainly ascribed to the borate groups, with small contributions coming from the Sr cations and OH groups. Detailed in this paper are the high yield synthesis, size-dependent SHG effect, phase matching property, UV transparency, thermal stability characterized by TG, DSC and variable-temperature PXRD, and theoretical studies on $Sr_2B_5O_9(OH)\cdot H_2O$.

2 Experimental

2.1 Synthesis

Analytically pure $Sr(OH)_2\cdot 8H_2O$, H_3BO_3 and NaOH, and distilled water were received from commercial sources. The title crystal was synthesized by a facile hydrothermal reaction. A mixture of $Sr(OH)_2\cdot 8H_2O$ (0.2658 g, 1 mmol), H_3BO_3 (0.1855 g, 3.0 mmol), NaOH (0.080 g, 2.0 mmol) and distilled water (10 mL) was sealed in an autoclave equipped with a teflon liner (23 mL). Then the autoclave was heated at 200 °C for 3 days and cooled down to room temperature (RT) at a rate of 2 °C/h. After that, the tefllon liner was opened in air and colorless block crystals were recovered, washed with distilled water, and dried overnight at RT. The product can also be obtained through the "Teflon-pouch method."[30,31]

2.2 Characterizations

Powder X-ray Diffraction (PXRD) data were collected on a Bruker D2 ADVANCE X-ray diffractometer with graphite-monochromatic Cu Kα radiation (λ = 1.5418 Å). The 2θ range was 10 - 70 ° with a step size of 0.02 ° and a fixed counting time of 1 s per step.

IR spectrum was recorded on a Shimadzu IR Affinity-1 Fourier transform Infrared spectrometer within the range 400 - 4000 cm^{-1} by using KBr pellets.

Optical diffuse reflectance spectrum was measured on a Shimadzu SolidSpec-3700DUV spectrophotometer at RT. Data were collected in the wavelength range 190 - 2600 nm. Reflectance spectrum was converted to absorbance using the Kubelka-Munk function.[32]

Thermal gravimetric (TG) analysis and differential scanning calorimetry (DSC) were carried out on a NETZSCH STA 449F3 thermal analyzer instrument at a temperature range 40 - 1000 °C with a heating rate of 5 °C min^{-1} in an atmosphere of flowing N_2.

Powder SHG measurement was performed on a modified Kurtz-NLO system using a pulsed Nd:YAG laser for excitation (1064 nm, 10 ns, 10 kHz).[33] Polycrystalline samples were ground and sieved into distinct particle size ranges (< 20, 20 - 38, 38 - 55, 55 - 88, 88 - 105, 105 - 150, and 150 - 200 μm). The microcrystallines of KDP were sieved into the same particle size ranges serving as a reference. Further details about the equipment and methodology have been published.[28]

Methodology on the single crystal X-ray diffraction measurement is given in ESI†. Relevant crystallographic data, atomic coordinates and thermal parameters, and selected bond lengths and angles for $Sr_2B_5O_9(OH)\cdot H_2O$ are given in Tables S1, S2 and S3, ESI†, respectively.

2.3 Computational Descriptions

Geometry optimization, electronic structure and optical property calculations were carried out on the basis of the DFT method implemented in the CASTEP package.[34] The convergence criteria applied for geometry optimization were 5.0 $\times$ 10^{-6} eV/atom for energy, 0.01 eV/Åfor force and 5.0 $\times$ 10^{-4} Åfor displacement. All subsequent calculations were performed on the optimized geometry. The norm-conserving pseudopotential[35,36] was used to describe the interactions between the ionic cores. A generalized gradient approximation of the Perdew-Burke-Ernzerhof scheme[37] was employed to describe the exchange-correlation XC function. The number of plane waves included in the basis set was determined by a cutoff energy of 830 eV. The numerical integration of the Brillouin zone was performed using Monkhorst-Pack *k*-point sampling of 3 $\times$ 3 $\times$ 5. The optical properties were then calculated based on the electronic structure obtained.

The refractive index was calculated by the equation, $N = n + ik$. n and k are obtained from equations, $n^2 = 1/2([\varepsilon_1{}^2 + \varepsilon_2{}^2]^{1/2} + \varepsilon_1)$ and $k^2 = 1/2([\varepsilon_1{}^2 + \varepsilon_2{}^2]^{1/2} - \varepsilon_1)$, respectively, where ε_1 and ε_2 are the real and imaginary parts of the dielectric constant, which were obtained using the OptaDOS code.[38]

The SHG tensors were calculated using the length-gauge formalism at a zero frequency limit.[39,40] The static second-order coefficients can be written as

$$\chi^{(2)}_{\alpha\beta\gamma} = \chi^{(2)}_{\alpha\beta\gamma}(VE) + \chi^{(2)}_{\alpha\beta\gamma}(VH) \quad (1)$$

In this formalism, the total SHG coefficient $\chi^{(2)}$ is divided into the contributions from the processes of virtual-electron transitions (VE) and virtual-hole transitions (VH). The contributions from VE and VH are calculated by the following formulas,

$$\chi^{(2)}_{\alpha\beta\gamma}(VE) = \frac{e^3}{2\hbar m^3}\sum_{vcc'}\int\frac{d^3k}{4\pi^3}P(\alpha\beta\gamma)Im[P^{\alpha}_{cv}P^{\beta}_{cc'}P^{\gamma}_{c'v}] \times\left(\frac{1}{\omega^3_{cv}\omega^2_{vc'}}+\frac{2}{\omega^4_{vc}\omega_{c'v}}\right) \quad (2)$$

$$\chi^{(2)}_{\alpha\beta\gamma}(VH) = \frac{e^3}{2\hbar m^3}\sum_{vv'c}\int\frac{d^3k}{4\pi^3}P(\alpha\beta\gamma)Im[P^{\alpha}_{vv'}P^{\beta}_{cv'}P^{\gamma}_{cv}] \times\left(\frac{1}{\omega^3_{cv}\omega^2_{v'c'}}+\frac{2}{\omega^4_{vc}\omega_{cv'}}\right) \quad (3)$$

where α, β and γ are Cartesian components, v and v' denote valence bands, c and c' refer to conduction bands, and $P(\alpha\beta\gamma)$ denotes full permutation. The band energy difference and momentum matrix elements are denoted as $\hbar\omega_{ij}$ and $P_{ij}{}^{\alpha}$, respectively.

The SHG-weighted electron density analysis was performed to identify the contribution of the orbitals or bands to the seconder order susceptibility. In this scheme, the considered SHG coefficient is resolved onto each orbital or band by keeping fixed one of the three band indexes for VE, VH and two-band transitions and summing the others. Based on this SHG weight, only the quantum states relevant to SHG are shown in the occupied or unoccupied SHG-density, which represents a highlight of the origin of SHG in real space. More details about the SHG-weighted electron density analysis have been published.[41]

The real-space atom-cutting analysis[42] was carried out in order to understand the respective contributions of the structural units. The cutting radii of Sr, B, O, H were set as 1.2, 0.7, 0.7 and 0.2 Å, respectively, with the restriction that the cutting spheres were in contact and not overlap.

3 Results and discussion

3.1 Synthesis

The title crystal was found to be sensitive to the mineralizer used in the reaction system. It can be obtained when NaOH mineralizer was added with an amount of 1, 2 and 3 mmol, respectively, whereas more NaOH (in our experiment, 4 and 5 mmol, respectively) led to the productions of $Sr(OH)_2{\cdot}8H_2O$ and an undetermined phase. However, the addition of KOH produced the crystal $SrBO_2(OH)$ (space group *Pnma*, CCDC reference number 174294) or $Sr(OH)_2{\cdot}8H_2O$. In our experiment, no crystal was obtained under the same reaction condition if there was no mineralizer added.

The title crystal was obtained in nearly quantitative yield based on Sr when 2 mmol NaOH was added. During repeated experiments, a crystal with size up to 6 × 2 × 2 mm^3 was obtained (Fig. S1, ESI†). It is suggested that $Sr_2B_5O_9(OH){\cdot}H_2O$ owns an excellent growth habit and large-size single crystals can be grown by the hydrothermal method. The purity of the microcrystalline product was identified by PXRD (Fig. 1, curves a and b).

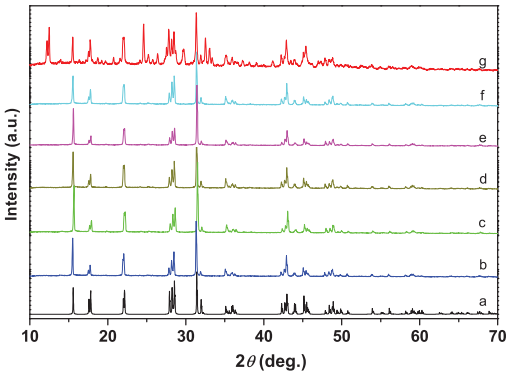

Fig. 1 XRD curves of $Sr_2B_5O_9(OH){\cdot}H_2O$: a, calculated; b, unannealed; c, annealed at 250 °C, 1h; d, annealed at 300 °C, 1h; e, annealed at 400 °C, 1h; f, annealed at 500 °C, 1h; g, annealed at 550 °C, 1h.

3.2 Crystal structure

The fundamental building block (FBB) of $Sr_2B_5O_9(OH){\cdot}H_2O$ is B_5O_{12} double-ring with each ring consisting of a central BO_4 tetrahedron, a non-central BO_4 tetrahedron and a BO_3 triangle sharing corners with each other (written as $2\triangle3T{:}\langle\triangle2T\rangle$-$\langle\triangle2T\rangle$ as suggested by Christ and Clark[43], Fig. 2(a)). The FBBs are *d*-type ones according to the definition of Ghose,[44] and form $(B_5O_{11})^{7-}$ chains by sharing O4 atoms along the *c* axis (Fig. 2(a)). The chains connect with each other by sharing O1 atoms along the *a* and *b* axes, respectively, extending to a three-dimensional $(B_5O_9)^{3-}$ framework (Fig. 2(b)) with the Sr^{2+}, OH^- and H_2O located in the channels (Fig. 2(c)). The Sr1 atoms are 9-coordinate with Sr-O distances in the range 2.558 - 2.903 Å(average = 2.658 Å). The specific coordination environment of the Sr1 atom was shown in Fig. 2(d).

Special attentions have been paid to the estimate the positions of hydrogen atoms geometrically, since improper positions of hydrogen atoms would led to unreasonable results for theoretical calculations. Bond valence sum (BVS) calculations[45,46] were performed for all atoms, which gave values of 2.1 for Sr1 atoms, 3.0 for B1, B2 and B3 atoms, and 2.0 for O1, O2, O3, O5, and O6 atoms, respectively (see Table S2, ESI†). These values are consistent with the expected valences. O4 are identified to be hydrogenated atoms because of their much smaller BVS values (0.6) without hydrogen. The very

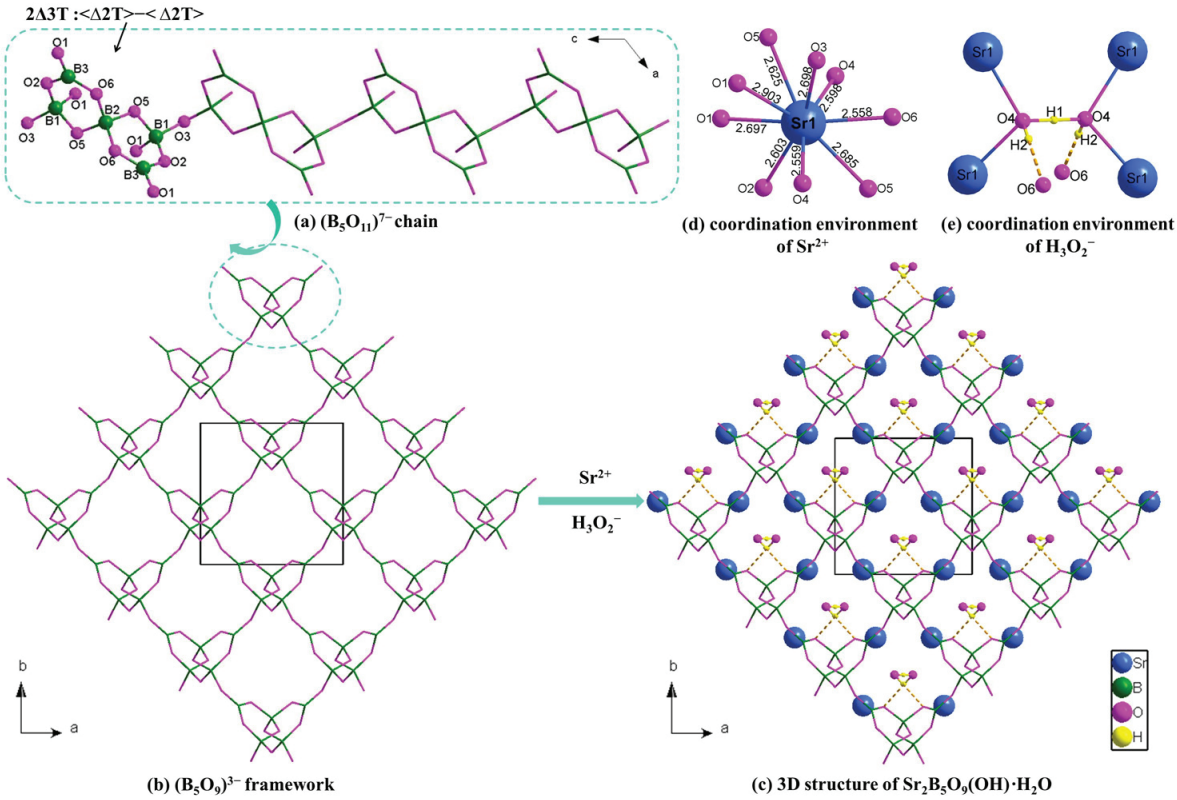

Fig. 2 Crystal structure of $Sr_2B_5O_9(OH)\cdot H_2O$.

short inter-atomic O4···O4 distance (2.480 Å) indicates that there exist a symmetrical hydrogen bond, O4-H1-O4, through which a $H_3O_2^-$ group has been formed. Therefore, during the structural refinement process, the H1 atom was placed in the centered position between O4···O4. Then the H2 atom was determined by considering the stereo-hindrance of the two strongly coordinating Sr1 atoms and the most preferential hydrogen bond acceptors (O6). The bond length of O4-H2 was estimated by the bond valence-bond length equation and bond valence parameters proposed for O-H···O bonds in inorganic crystals.[47] The coordination environment of the $H_3O_2^-$ group and the configuration of the special symmetrical hydrogen bond were illustrated in Fig. 2(e).

The DFT geometry optimization resulted in unit cell parameters of a = 10.3068 Å, b = 8.0447 Å, c = 6.4249 Å, β = 127.4013 °, which are consistent with the cell parameters obtained from experiment. Specifically, the root mean square deviations for the bond lengths of B-O, Sr-O and O-H bonds in the unit cell are 0.01, 0.03 and 0.05, respectively. The numerical refined hydrogen bond lengths and angles (Table S3), Mulliken analysis and electron density calculations are given in ESI†.

3.3 IR Spectroscopy

The IR spectrum conforms the presence of the structural units (Fig. S2, ESI†). It displays strong absorption bands around 1250 - 1500 cm^{-1} which can be assigned to the asymmetric stretching vibrations of the BO_3 groups. The bands centered at 1120 and 960 cm^{-1} are likely the asymmetric and symmetric stretching for the BO_4 groups. The bending vibrations of BO_3 and BO_4 are also shown in 500 - 800 cm^{-1}. The IR spectrum also clearly confirms the presence of the OH^- groups in the material by the broad absorption peak centered around 3500 cm^{-1}.

3.4 UV-Vis-NIR Diffuse Reflectance Spectroscopy

The UV-Vis-NIR diffuse reflectance spectroscopy is of critical concern because the application range of the NLO crystal was greatly restricted by its transparency window. Fig. 3 is the UV-Vis-NIR diffuse reflectance spectrum for $Sr_2B_5O_9(OH)\cdot H_2O$. It clearly shows a wide transparency range from deep UV to NIR with a short-wavelength cutoff edge lower than 190 nm, which indicates that it can be used in the UV range. The inset of Fig. 3 shows the absorption (K/S) data that calculated

from the Kubelka-Munk function.[32] In the $F(R)^2$-E plot, extrapolating the linear part of the rising curve to zero provides an approximate band gap of 5.9 eV.

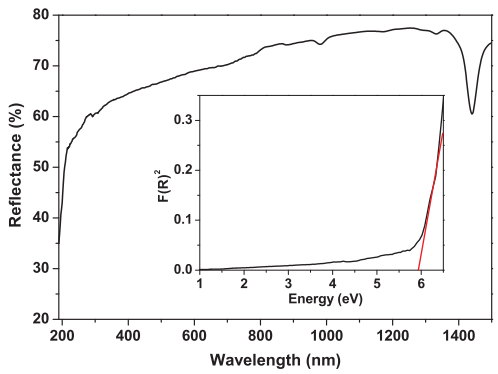

Fig. 3 UV-Vis-NIR diffuse reflectance spectrum of $Sr_2B_5O_9(OH)\cdot H_2O$ showing a transparency range from UV to NIR and an approximate band gap of 5.9 eV.

3.5 SHG Effect

Moderate green-light output was observed from the ground samples on illumination with 1064 nm light. Fig. 4 shows the SHG signal intensity versus particle size. It is clearly shown that the SHG signal intensity increases with the particle sizes and plateaus at a maximum value, which indicates that the material is phase-matchable according to the rule proposed by Kurtz and Perry.[33] Comparison of the SHG signal intensity produced by $Sr_2B_5O_9(OH)\cdot H_2O$ sample with that of KDP sample in the same particle range reveals that it exhibits a SHG response of approximately 3 times that of KDP (see inset in Fig. 4) which is comparable to that of $Sr_4B_{10}O_{18}(OH)_2\cdot 2H_2O$.[28]

3.6 Thermal Analysis

TG and DSC combined with PXRD for a sample underwent annealing at different temperatures were measured to investigate the thermal property of $Sr_2B_5O_9(OH)\cdot H_2O$. Results of TG studies (Fig. 5) indicate that $Sr_2B_5O_9(OH)\cdot H_2O$ is stable up to 500 °C. Upon further heating, the crystalline water and hydroxyl groups start to decompose with weight loss that ends at 600 °C. These assignments are in agreement with the endothermic peak at 520 °C in the DSC diagram (Fig. 5). The total weight loss of 6.2 % is close to the calculated value of 6.6 % corresponding to the release of 1.5 mol of water molecules per formula unit.

Fig. 1(c-g) also collects XRD curves recorded for the sample annealed for 1 h in an oven at 250, 300, 400, 500, and 550 °C , respectively. The profile (f) (annealed at 500 °C for 1 h) is similar to (b) (unannealed), indicating that no significant changes occur in the crystal phase in the temperature range RT to 500 °C. And we also observed SHG (green light, frequency at 532 nm) from these samples irradiated with the Nd:YAG laser. In the profile (g) (annealed at 550 °C for 1 h), new reflections appeared, indicating that some unknown new phases were produced. This PXRD result agrees well with the decompose phenomenon (T = 520 °C) detected in TG and DSC curves.

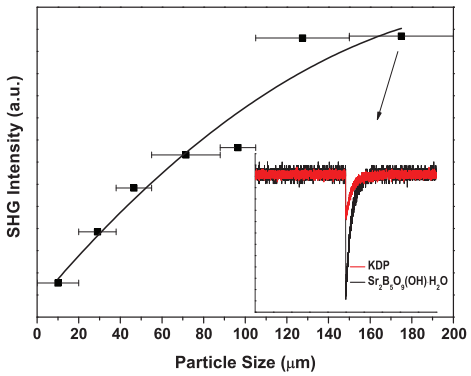

Fig. 4 The dependency of SHG intensity on particle size for $Sr_2B_5O_9(OH)\cdot H_2O$. The curve is drawn to guide the eye and is not a fit to the data. Inset are the oscilloscope traces of the SHG signals for the samples of $Sr_2B_5O_9(OH)\cdot H_2O$ and KDP with particle sizes in the range 150 - 200 μm.

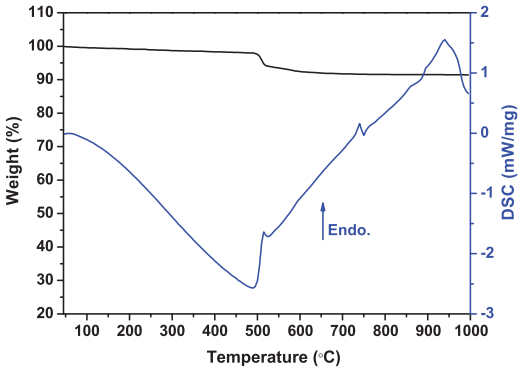

Fig. 5 TG and DSC data for $Sr_2B_5O_9(OH)\cdot H_2O$. The TG curve (black solid line) shows no weight loss up to about 500 °C. In the DSC curve (blue solid line), an endothermic peak during the heating process at about 520 °C is observed.

3.7 Optical Properties Analyses

The electronic band structure of $Sr_2B_5O_9(OH)\cdot H_2O$ is shown in Fig. 6(a). It is shown that $Sr_2B_5O_9(OH)\cdot H_2O$ is a direct gap compound with a calculated band gap of 5.56 eV. It is slightly smaller than the experimentally determined value, 5.9

eV. Fig. 6(b) shows the total density of states (TDOS) and projected density of states (PDOSs) between − 7.5 and 15 eV. It is clearly shown that the band from − 7.5 to − 2.5 eV is dominated mainly by O-2*p* and B-2*p* orbitals, and slightly by H-1*s* orbitals. The narrow band from − 2.5 eV to the Fermi level is mainly composed of O-2*p* orbitals mixing with small amount of Sr-(5*s*, 4*d*) orbitals. The band from 5 to 11 eV mainly consists of B-2*p* and Sr-4*d* orbitals with very small contributions from the O-2*p*, H-1*s* and Sr-5*s* orbitals.

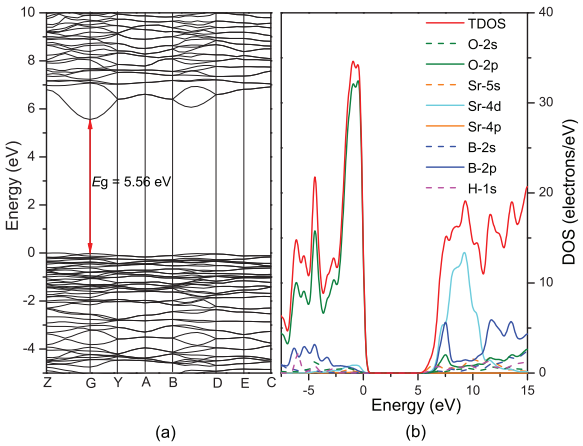

Fig. 6 The electronic band structure of $Sr_2B_5O_9(OH)\cdot H_2O$. The arrow indicates the direct band gap (a); TDOS and PDOSs of $Sr_2B_5O_9(OH)\cdot H_2O$ (b). The Fermi level is set as $E = 0$ eV.

In order to resolve the individual atomic contributions, additional detailed PDOSs analyses were performed. Fig. 7 reveals the PDOSs of O-(2*s*, 2*p*), B-(2*s*, 2*p*), H-1*s* and Sr-(5*s*, 4*d*, 4*p*) between − 7.5 and 15 eV, respectively. Since most optical properties of a compound are determined by the valence electrons, which mainly contribute to the band structures in the vicinity of Fermi level, a closer investigation on that range is necessary. In the B-PDOS, significant contribution of the B3-2*p* orbital appears at 7.5 eV in the bottom of the conduction band whereas contributions of the 2*p* orbitals of B1 and B2 are farther from the band gap which located in the range 10 - 15 eV. It is indicated that the optical properties of the compound mainly come from the BO_3 groups, which is consistent with the anionic group theory that identified the important contributions of the π-conjugated BO_3 groups to the NLO properties in borates. It is interesting to note that there are also small contributions of H2-1*s* and Sr1-5*s* orbitals appearing at 7.5 eV. In addition, the sharp peak at 7.5 eV in the PDOSs of O is dominated by 2*p* orbitals of O4 and O5, whereas contributions of 2*p* orbitals of O1, O2, O3, and O6 atoms are farther from the Fermi level. Therefore, one can deduce that the O4-H2 and the Sr1-O5 groups would also give some contributions to the optical properties.

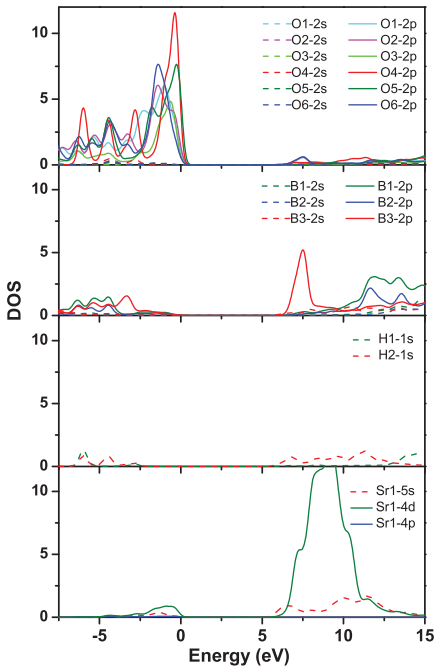

Fig. 7 Detailed PDOSs of $Sr_2B_5O_9(OH)\cdot H_2O$. The Fermi level is set as $E = 0$ eV.

The dispersions of the linear refractive indices were calculated on the basis of the electronic structure and the birefringence in the wavelength region 400 - 1100 nm was shown in Fig. 8. In the region 532 - 1064 nm the calculated birefringence is about 0.053 - 0.049.

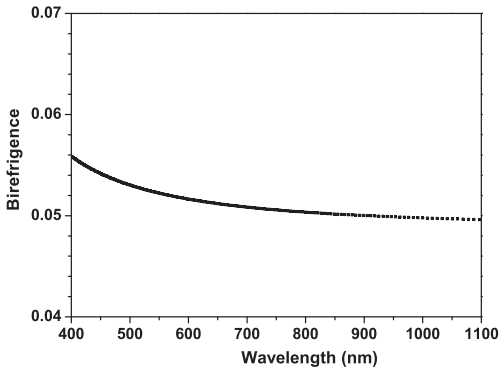

Fig. 8 The calaulated birefringence of $Sr_2B_5O_9(OH)\cdot H_2O$ in the wavelength region 400 - 1100 nm.

According to the group symmetry and Kleinman approximation of point group 2, the crystal has four non-zero NLO coefficients, i.e., d_{14} (= d_{25} = d_{36}), d_{16} (= d_{21}), d_{22} and d_{23} (= d_{34}). The calculated values of d_{14}, d_{16}, d_{22} and d_{23} are − 0.81, 1.05, − 0.37, and − 0.74 pmV^{-1}, respectively, with the

largest value being 2.7 times that of KDP (d_{36} = 0.39 pmV^{-1}). It is consistent well with the experimental results.

Fig. 9 shows the SHG-density of the *VE* transition process, which gives the dominant contribution to the largest SHG tensor d_{16} (about 78.8 %). It clearly shows that the occupied states contributed to d_{16} mainly come from the O-2*p* orbitals, while the unoccupied states mainly come from the B3-2*p* orbitals with small contributions from the conduction bands of O-2*p*. It is indicated that the *VE* process from the O valence state to the B3 conduction states determine the SHG effect in the title crystal. Compared to B3 that is three coordinated to oxygen atoms, contributions from other cations, i.e., four coordinated B atoms, Sr and H cations, are much smaller.

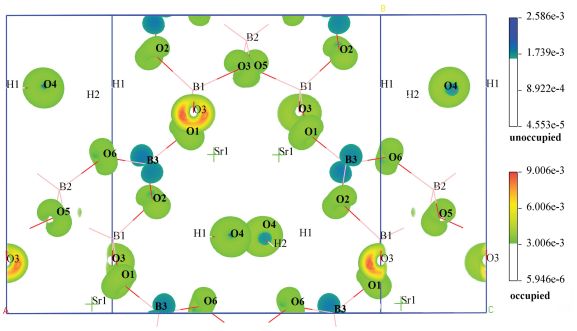

Fig. 9 SHG-weighted electron densities of the occupied and unoccupied orbitals in the *VE* process of the SHG tensor d_{16} of $Sr_2B_5O_9(OH)\cdot H_2O$.

In order to further quantitatively understand the respective contributions of the structural units, i.e., the $(B_5O_9)^{3-}$ framework, the Sr^{2+} cations, and $H_3O_2^-$ groups to the optical response, real-space atom-cutting analysis was carried out. The results are given in Table 1. It clearly shows that the SHG response mainly comes from the borate group whose contributions account for 80.3 %, 55.2 %, 62.2 % and 58.1 % for the SHG tensors d_{14}, d_{16}, d_{22} and d_{23}, respectively. Though the SHG contributions of the Sr cations and the O-H groups are smaller than those from B-O groups, they cannot be neglected. For instance, as shown in Table 1, the SHG contributions of Sr cations and O-H groups for tensor d_{16} account for 30.5 % and 13.3 %, respectively. The similarly relative large contributions of the alkaline-earth cations and the O-H groups have also been observed in $Sr_4B_{10}O_{18}(OH)_2\cdot 2H_2O$.[28] It is suggested that alkaline-earth cations and O-H groups play important roles in the NLO properties and can be employed as NLO functional building blocks for materials design.

4 Conclusions

$Sr_2B_5O_9(OH)\cdot H_2O$ is synthesized in high yields under hydrothermal conditions. The structure features a three-dimensional (B_5O_9) framework composing by *d*-type B_5O_{12} double-ring FBBs. H_2O molecules and OH^- groups locate in the channels of the framework forming symmetrical hydrogen bonds that are rare in inorganic structures. The compound possesses a wide transparency from the UV to NIR spectrum with UV cutoff edge below 190 nm. It is phase matchable and exhibits a powder SHG effect of approximately 3 times that of KDP. It also has high thermal stability up to 500 °C and a good growth habit. These features make $Sr_2B_5O_9(OH)\cdot H_2O$ very promising as UV NLO material. The calculated NLO coefficients give the largest value of 1.05 pmV^{-1} being 2.7 times that of KDP, which is consistent well with the experimental results. The electronic structure, SHG-weighted electron densities combined with the real-space atom-cutting analyses verify the dominating contributions of the borate groups to the SHG effect, as well as the distinct contributions of the alkaline-earth cations and OH groups.

Table 1 Contributions of different structural units to SHG coefficients estimated by real-space atom-cutting analysis

	d_{14}	d_{16}	d_{22}	d_{23}
$(B_5O_9)^{3-}$	− 0.65	0.58	−0.23	−0.43
Sr^{2+}	0.02	0.32	0.10	−0.11
$H_3O_2^-$	0.01	0.14	−0.02	−0.09
total	−0.81	1.05	−0.37	−0.74

5 Acknowledgements

This work was supported by the NSFC (Grant Nos. 21301189, 51425206, U1129301, 51172277), National Basic Research Program of China (Grant No. 2014CB648400), the West Light Foundation of CAS (Grant No. ZDXM-2014-01), the Foundation of the Youth Innovation Promotion Association of CAS, the Xinjiang International Science and Technology Cooperation Program (20146001), the Funds for Creative Cross and Cooperation Teams of CAS, Xinjiang Key Laboratory Foundation (Grant No. 2014KL009).

References

1 C. Chen, B. Wu, A. Jiang and G. You, *Sci. Sin., Ser. B*, 1985, **28**, 235-243.
2 C. Chen, Y. Wu, A. Jiang, B. Wu, G. You, R. Li and S. Lin, *J. Opt. Soc. Am. B*, 1989, **6**, 616-621.
3 Y. Wu, T. Sasaki, S. Nakai, A. Yokotani, H. Tang and C. Chen, *Appl. Phys. Lett.*, 1993, **62**, 2614-2615.
4 Y. Mori, I. Kuroda, S. Nakajima, T. Sasaki and S. Nakai, *Appl. Phys. Lett.*, 1995, **67**, 1818-1820.
5 L. Mei, Y. Wang, Q. Wu, B. Wu and C. Chen, *Z. Kristallogr.*, 1995, **210**, 93-95.
6 (a) H. Huang, L. Liu, S. Jin, W. Yao, Y. Zhang and C. Chen, *J. Am. Chem. Soc.*, 2013, **135**, 18319-18322; (b) H. Huang, J. Yao, Z. Lin, X. Wang, R. He, W. Yao, N. Zhai and C. Chen, *Angew. Chem. Int. Ed.*, 2011, **50**, 9141-9144.

7 (a) H. Wu, H. Yu, Z. Yang, X. Hou, X. Su, S. Pan, K. R. Poeppelmeier and J. M. Rondinelli, *J. Am. Chem. Soc.*, 2013, **135**, 4215-4218; (b) H. Wu, S. Pan, K. R. Poeppelmeier, H. Li, D. Jia, Z. Chen, X. Fan, Y. Yang, J. M. Rondinelli and H. Luo, *J. Am. Chem. Soc.*, 2011, **133**, 7786-7790; (c) Z. Huang, X. Su, S. Pan, X. Dong, S. Han, H. Yu, M. Zhang, Y. Yang, S. Cui and Z. Yang, *Scripta Mater.*, 2013, **69**, 449-452.

8 K. Xu, P. Loiseau and P. G. Aka, *J. Cryst. Growth*, 2009, **311**, 2508-2512.

9 (a) H. Wu, H. Yu, S. Pan, Z. Huang, Z. Yang, X. Su and K. R. Poeppelmeier, *Angew. Chem. Int. Ed.*, 2013, **52**, 3406-3410; (b) X. Lin, F. Zhang, S. Pan, H. Yu, F. Zhang, X. Dong, S. Han, L. Dong, C. Bai and Z. Wang, *J. Mater. Chem. C*, 2014, **2**, 4257-4264.

10 (a) K. Feng, W. Yin, W. Hao, J. Yao and Y. Wu, *CrystEngComm*, 2013, **15**, 5064-5069; (b) R. Arun Kumar and R. Dhanasekaran, *J. Cryst. Growth*, 2009, **311**, 541-543; (c) J. Yu, L. Liu, N. Zhai, X. Zhang, G. Wang, X. Wang and C. Chen, *J. Cryst. Growth*, 2012, **341**, 61-65.

11 (a) M. Luo, G. Wang, C. Lin, N. Ye, Y. Zhou and W. Cheng, *Inorg. Chem.*, 2014, **53**, 8098-8104; (b) M. Luo, N. Ye, G. Zou, C. Lin and W. Cheng, *Chem. Mater.*, 2013, **25**, 3147-3153.

12 (a) S. Zhao, P. Gong, S. Luo, L. Bai, Z. Lin, C. Ji, T. Chen, M. Hong and J. Luo, *J. Am. Chem. Soc.*, 2014, **136**, 8560-8563; (b) T. Sun, P. Shan, H. Chen, X. Liu, H. Liu, S. Chen, Y. Cao, Y. Kong and J. Xu, *CrystEngComm*, 2014, **16**, 10497-10504; (c) P. Yu, L. Wu, L. Zhou and L. Chen, *J. Am. Chem. Soc.*, 2013, **136**, 480-487.

13 J. F. Nye, Physical Properties of Crystals. Oxford University Press: Oxford, 1957

14 P. S. Halasyamani and K. R. Poeppelmeier, *Chem. Mater.*, 1998, **10**, 2753-2769.

15 C. Chen, Y. Wu and R. Li, *Int. Rev. Phys. Chem.*, 1989, **8**, 65-91.

16 E. L. Belokoneva, *Crystallogr. Rev.*, 2005, **11**, 151-198.

17 Z. Lin and G. Yang, *Eur. J. Inorg. Chem.*, 2011, **2011**, 3857-3867.

18 G. Yuan and D. Xue, *Acta Crystallogr. B*, 2007, **63**, 353-362.

19 (a) H. Huppertz and B. von der Eltz, *J. Am. Chem. Soc.*, 2002, **124**, 9376-9377; (b) G. Sohr, D. M. Toebbens, J. S.auf der Gunne and H. Huppertz, *Chem. Eur. J.*, 2014, **20**, 17059-17067; (c) H. Huppertz, *Z. Naturforsch., B: Chem. Sci.*, 2003, **58**, 278-290.

20 (a) C. Heyward, C. McMillen and J. Kolis, *Inorg. Chem.*, 2012, **51**, 3956-3962; (b) C. McMillen, C. Heyward, H. Giesber and J. Kolis, *J. Solid State Chem.*, 2011, **184**, 2966-2971; (c) H. Giesber, PhD dissertation, Clemson University, Clemson, SC, 2002; (d) C. McMillen, PhD dissertation, Clemson University, Clemson, SC, 2007.

21 Z. Yu, Z. Shi, W. Chen, Y. Jiang, H. Yuan and J. Chen, *J. Chem. Soc., Dalton Trans.*, 2002, **9**, 2031-2035.

22 Q. Lin, W. Cheng, J. Chen and J. Huang, *J. Solid State Chem.*, 1999, **144**, 30-34.

23 (a) N. L. Ross and R. J. Angel, *J. Solid State Chem.*, 1991, **90**, 27-30; (b) J.-B. Kim, K.-S. Lee, I.-H. Suh, J.-H. Lee, J.-R. Park and Y.-H. Shin, *Acta Crystallogr. C*, 1996, **52**, 498-500.

24 (a) Z. Tang, X. Chen and M. Li, *Solid State Sci.*, 2008, **10**, 894-900; (b) Z. Wei, X. Chen, F. Wang, W. Li, M. He and Y. Zhang, *J. Alloy. Compd.*, 2001, **327**, L10-L13.

25 (a) F. Pan, G. Shen, R. Wang, X. Wang and D. Shen, *Acta Crystallogr.*, 1966, **20**, 274-279.

26 (a) A. E. Lapshin, E. O. Litovchik, I. G. Polyakova and Y. F. Shepelev, *Russ. J. Inorg. Chem.*, 2007, **52**, 839-843; (b) D. P. Kudrjavtcev, Y. S. Oseledchik, A. L. Prosvirnin and N. V. Svitanko, *J. Cryst. Growth*, 2003, **254**, 456-460; (c) D. P. Kudrjavtcev, Yu. S. Oseledchik, A. L. Prosvirnin, N. V. Svitanko and V. V. Petrov, *Ukr. J. Phys. Opt.*, 2002, **2**, 155-160.

27 Q. Meng, G. Wang, J. Xue, B. Yang, H. He and G. Yang, *J. Clust. Sci.*, 2014, **25**, 1319-1329.

28 F. Zhang, Q. Jing, F. Zhang, S. Pan, Z. Yang, J. Han, M. Zhang, S. Han, *J. Mater. Chem. C*, 2014, **2**, 667-674.

29 J. Barbier and H. Park, *Can. Mineral.*, 2001, **39**, 129-135.

30 W. T. A. Harrison, T. M. Nenoff, T. E. Gier and G. D. Stucky, *Inorg. Chem.*, 1993, **32**, 2437-2441.

31 W. C. Sheets, E. Mugnier, A. Barnab, T. J. Marks and K. R. Poeppelmeier, *Chem. Mater.*, 2005, **18**, 7-20.

32 P. Kubelka and F. Munk, *Z. Tech. Phys.*, 1931, **12**, 593-601.

33 S. K. Kurtz and T. T. Perry, *J. Appl. Phys.*, 1968, **39**, 3798-3813.

34 J. Clark Stewart, D. Segall Matthew, J. Pickard Chris, J. Hasnip Phil, I. J. Probert Matt, K. Refson and C. Payne Mike, *Z. Kristallogr.*, 2005, **220**, 567-570.

35 J. P. Perdew, K. Burke and M. Ernzerhof, *Phys. Rev. Lett.*, 1996, **77**, 3865-3868.

36 J. Lin, A. Qteish, M. C. Payne and V. Heine, *Phys. Rev. B*, 1993, **47**, 4174-4180.

37 A. M. Rappe, K. M. Rabe, E. Kaxiras, J. D. Joannopoulos, *Phys. Rev. B*, 1990, **41**, 1227-1230.

38 A. J. Morris, R. J. Nicholls, C. J. Pickard and J. R. Yates, *Comput. Phys. Commun.*, 2014, **185**, 1477-1485.

39 C. Aversa and J. E. Sipe, *Phys. Rev. B*, 1995, **52**, 14636-14645.

40 B. Zhang, M.-H. Lee, Z. Yang, Q. Jing, S. Pan, M. Zhang, H. Wu, X. Su and C.-S. Li, *Appl. Phys. Lett.*, 2015, **106**, 031906.

41 Q. Jing, X. Dong, Z. Yang, S. Pan, B. Zhang, X. Huang and M. Chen, *J. Solid State Chem.*, 2014, **219**, 138-142.

42 J. Lin, M.-H. Lee, Z.-P. Liu, C. Chen and C. J. Pickard, *Phys. Rev. B*, 1999, **60**, 13380-13389.

43 C. L. Christ and J. Clark, *Phys. Chem. Minerals*, 1977, **2**, 59-87.

44 S. Ghose, *Am. Mineral.*, 1982, **67**, 1265-1272.

45 I. D. Brown and D. Altermatt, *Acta Crystallogr. B*, 1985, **41**, 244-247.

46 N. E. Brese and M. O'Keeffe, *Acta Crystallogr. B*, 1991, **47**, 192-197.

47 F. Zhang, K. Li, H. Ratajczak and D. Xue, *J. Mol. Struc.*, 2010, **976**, 69-72.